Quantitative Assessment of Optical Gain and Loss in Submicron-Textured $CuIn_{1-x}Ga_xSe_2$ Solar Cells Fabricated by Three-Stage Coevaporation

Takuya Hara,[1] Takuji Maekawa,[2] Shota Minoura,[1] Yuichiro Sago,[1] Shigeru Niki,[3] and Hiroyuki Fujiwara[1*]

[1]*Center of Innovative Photovoltaic Systems (CIPS), Gifu University, 1-1 Yanagido, Gifu 501-1193, Japan*

[2]*Research and Development Headquarters, ROHM Co., Ltd., 21 Saiin Mizosaki-cho, Ukyo-ku, Kyoto 615-8585, Japan*

[3]*Research Center for Photovoltaic Technologies, National Institute of Advanced Industrial Science and Technology (AIST), Central2, 1-1-1 Umezono, Tsukuba, Ibaraki 305-8568, Japan*

(Received 4 June 2014; published 29 September 2014)

The external quantum efficiency (EQE) spectra of high-efficiency $CuInGaSe_2$ (CIGS)-based solar cells fabricated by a standard three-stage process are simulated by incorporating the effects of (i) the V-shaped Ga-compositional profile within a 1.8-μm-thick CIGS layer and (ii) the light scattering caused by the submicron-textured structure. For the EQE calculation of the CIGS solar cells, we develop a simulation scheme in which the total light absorption in the solar cell is assessed using the experimental reflectance spectrum, whereas the absorptance of each solar-cell layer is deduced by assuming a flat optical model. The optical effect of the double-graded Ga-compositional profile in the CIGS layers is calculated explicitly based on a complete CIGS optical database established recently. A highly accurate EQE simulation for CIGS solar cells is made possible by the developed simple calculation method. In particular, our technique allows the determination of the partial EQE contributions for different thicknesses and wavelengths in the CIGS-based solar cells. The EQE analysis reveals that the carrier collection efficiency in the CIGS light-absorber layers is almost unity, but the light absorption in the 1-μm-thick CIGS bottom region is negligible, confirming that the bottom layer with higher Ga content plays a dominant role as a back-surface field with the conduction-band grading. We find that the major optical loss occurs in the ZnO:Al, CdS, and Mo component layers with a corresponding current loss of approximately 3 mA/cm^2 in each layer. Furthermore, an EQE simulation method for arbitrary CIGS solar-cell structures is developed by imposing the antireflection condition in the calculation of the reflectance spectra. By applying this technique, the effects of the Ga-compositional profiles and thicknesses of various solar-cell component layers on the EQE spectrum are determined.

DOI: 10.1103/PhysRevApplied.2.034012

I. INTRODUCTION

For $CuIn_{1-x}Ga_xSe_2$ (CIGS)-based solar cells with a high efficiency exceeding 20% [1–3], a three-stage coevaporation process in which (Cu, In, Ga, Se) elemental sources are supplied with different combinations [4–6] is commonly employed. In particular, using this process, a V-shaped Ga-compositional profile is generated within the CIGS light-absorber layer, which is essential for realizing a high short-circuit current density (J_{SC}), while maintaining a high open-circuit voltage (V_{OC}) in CIGS solar cells [1–8]. Because of the complexity of the CIGS structures, the development of an optical simulation technique can give a crucial contribution to the interpretation of numerous quantum efficiency spectra and the resulting J_{SC} values reported for CIGS solar cells [1–36]. Nevertheless, the optical simulation of CIGS solar-cell devices is rather difficult because of (i) the light-scattering effect induced by submicron-size CIGS natural textures and (ii) the continuous variation of the Ga content in the CIGS layer [1–8].

Although light scattering on rough surfaces can be estimated by using computer-intensive methods including the rigorous coupled-wave analysis [37], the ray-tracing method [38], the field-integration technique [39,40], and the finite-element method [41], the optical simulation of thin-film solar cells by such methods is generally quite time consuming and sometimes difficult. Specifically, in these calculations, proper modeling of the three-dimensional random structures is necessary for all the interfaces in the multilayer-device structures, so that the light absorption and reflection in solar cells are reproduced with high accuracy. Unfortunately, the external quantum efficiency (EQE) spectra obtained from such approaches still need to be justified by comparing them with the experimental spectra, in part due to limited computer resources for the geometric modeling. Moreover, in the case of CIGS solar cells, the topological features of the surface and interface depend strongly on device preparation conditions [36]. Thus, an EQE

*fujiwara@gifu-u.ac.jp

simulation based on exact modeling of surface and interface structures may have limited practical use.

To perform an optical simulation of CIGS devices, on the other hand, appropriate optical constants are required for all the solar-cell component layers. For the change in $CuIn_{1-x}Ga_xSe_2$ optical constants with x, however, different optical spectra have been reported [42–48]. Because of the above difficulties, only limited optical simulations have been performed for CIGS solar cells so far [5,8–18]. To further improve the efficiency of CIGS-based solar cells, it is vital to determine the intrinsic factors that limit the EQE response and J_{SC} in the solar cells.

In this paper, for high-precision EQE characterization of submicron-textured CIGS solar cells, we develop a scheme in which the light absorption in the solar cell is calculated by assuming a completely flat structure, whereas the contribution of the scattered light is incorporated by adopting an experimental reflectance spectrum obtained from the textured structure. In our technique, therefore, the total light absorption in the whole solar-cell structure is determined from the actual device, and the absorptance in each solar-cell component layer is deduced from the conventional optical-admittance method, which uses a flat optical model [49–51]. In the simulation, the optical response of the CIGS layer with a double-gradient Ga structure is calculated explicitly using a complete CIGS optical database that was established recently [48]. In particular, we previously found that the absorption coefficient of $CuInSe_2$ (CIS) is only $\alpha = 6.6 \times 10^4$ cm^{-1} at 2.0 eV when the effect of the surface roughness is removed almost completely [48]. This α value is far smaller than the value widely cited [52] ($\alpha = 1.7 \times 10^5$ cm^{-1} at 2.0 eV), and in the optical simulation of this work, the accurate optical constants of the CIGS layers are applied.

As a result, we confirm that the EQE spectra of CIGS-based solar cells fabricated by a standard three-stage process can be reproduced quite well using the developed method. From this technique, a quantitative description of the optical loss and gain in CIGS solar cells becomes possible. Moreover, for the EQE simulation of different CIGS structures, we develop a formalism in which the reflectance spectrum is calculated by imposing the antireflection condition in the multilayer structure. We demonstrate that our simple approach allows an EQE simulation of various CIGS solar-cell structures with sufficient accuracy.

II. EXPERIMENT

For the fabrication of CIGS solar cells, we form a multilayer structure of MgF_2/ZnO:Al/ZnO/CdS/CIGS/Mo/soda-lime glass substrate with an Al-grid front electrode on the ZnO:Al. The CIGS layers are prepared by a standard three-stage process [4–6] using temperatures of 400 °C for the first stage and 520 °C for the second and third stages. Prior to the deposition of the CdS layers, potassium cyanide (KCN) treatments [53,54] are performed for the deposited CIGS layers, and the CdS layers are then prepared by a standard chemical-bath deposition (CBD) technique [55]. We fabricate the nondoped-ZnO, Al-doped ZnO, and Mo layers by sputtering, whereas the Al-grid electrode and MgF_2 antireflective coating are formed using thermal-evaporation systems. To measure the reflectance spectra of the solar cells, we prepare similar solar-cell structures from the same batch as the actual solar-cell fabrication, without forming the Al front electrode.

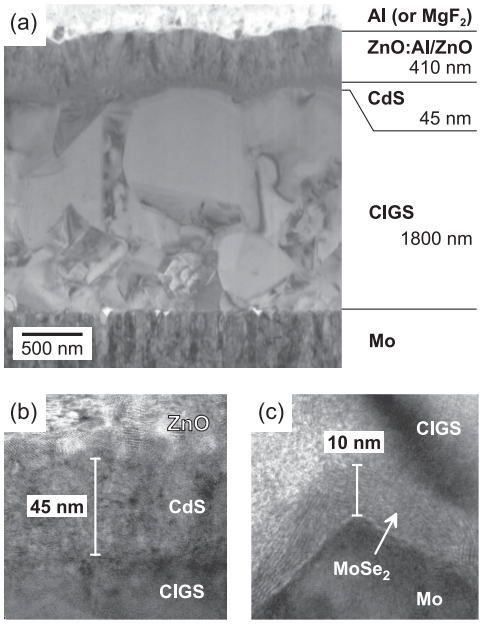

FIG. 1. Cross-sectional TEM images obtained from the CIGS solar cell fabricated in this work: (a) the whole solar-cell structure in the region with the Al electrode, (b) the enlarged image for the ZnO/CdS/CIGS interface, and (c) the enlarged image for the CIGS/Mo interface.

Figure 1 shows the cross-sectional transmission electron microscopy (TEM) images obtained from the CIGS solar cell fabricated in this work: (a) the whole solar-cell structure in the region with the Al electrode, (b) the enlarged image for the ZnO/CdS/CIGS interface, and (c) the enlarged image for the CIGS/Mo interface. In the TEM image, the formation of large CIGS grains with a size of approximately 1 μm can be seen. As shown in Fig. 1, the CdS layer covers the CIGS layer uniformly with a thickness of 45 nm. The TEM reveals the presence of a thin $MoSe_2$ layer with a maximum thickness of 11 nm at the CIGS/Mo interface, as reported previously [15,56]. The conversion efficiency of the CIGS solar cell in Fig. 1 is 16.7% with $J_{SC} = 34.2$ mA/cm^2, $V_{OC} = 674$ mV, and a fill factor of FF = 0.725.

III. SIMULATION METHOD

A. EQE calculation

For the calculation of the absorptance spectra corresponding to each solar-cell component layer, we apply the

conventional optical-admittance method [49–51]. Figure 2 shows (a) the calculation procedure in the optical-admittance method, (b) the light reflection and transmission in a textured structure, and (c) the optical model used for the analysis of the CIGS solar cells. The N_j, Y_j, ψ_j, and d_j in Fig. 2(a) denote the complex refractive index, optical admittance, potential transmittance, and thickness of the jth layer, respectively, and $j = 0$ represents the ambient environment (air). The N_j is defined from the refractive index n and the extinction coefficient k as $N_j = n_j - ik_j$. In Fig. 2(a), R_{flat} indicates the reflectance in the flat layered structure when the light intensity is $I = 1$.

The optical admittance is defined by $Y = H_f/E_f$, where H_f and E_f show the magnetic and electric fields, respectively. Since $H_f = nE_f$ in the case of nonabsorbing media, Y basically represents N, and the optical admittance of the substrate is given by $N_{j+1} = Y_j$. In the multilayer structure of Fig. 2(a), by satisfying the electromagnetic boundary conditions at the interfaces, Y_j can be transferred to Y_{j-1} according to

$$Y_{j-1} = \frac{Y_j \cos(\delta_j) + iN_j \sin(\delta_j)}{\cos(\delta_j) + iY_j \sin(\delta_j)/N_j}, \tag{1}$$

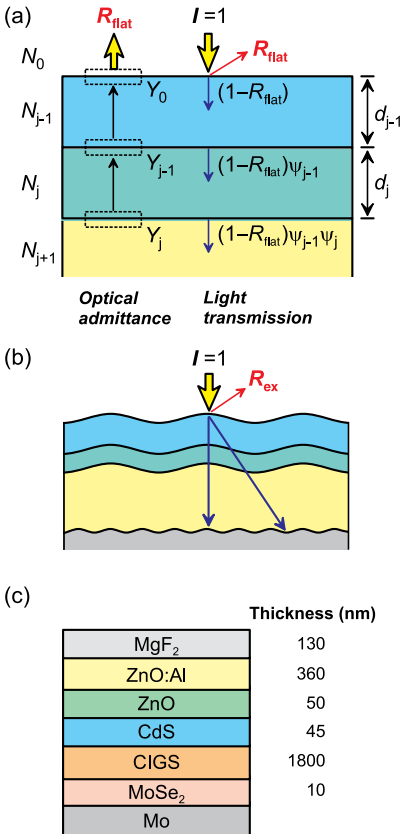

FIG. 2. (a) Calculation procedure in the optical-admittance method, (b) light reflection and transmission in a textured structure, and (c) optical model used for the analysis of the CIGS solar cell.

where δ_j shows the phase thickness expressed by $\delta_j = 2\pi N_j d_j/\lambda$. Here, λ is the wavelength of light. By repeating the process of Eq. (1) in the multilayer structure, Y_0 is determined and, from this value, R_{flat} is calculated simply as

$$R_{\text{flat}} = |1 - Y_0|^2/|1 + Y_0|^2. \tag{2}$$

In the optical-admittance method, the light transmittance T at each interface can be obtained by multiplying ψ of each layer sequentially from the top layer. In Fig. 2(a), ψ_j is given by

$$\psi_j = \frac{\text{Re}(Y_j)}{\text{Re}(Y_{j-1})|\cos(\delta_j) + iY_j \sin(\delta_j)/N_j|^2}. \tag{3}$$

From R_{flat} and ψ of each layer, the absorptance in the jth layer (A_j) is determined from

$$A_j = (1 - R_{\text{flat}})(1 - \psi_j)\prod_{k=1}^{j-1}\psi_k. \tag{4}$$

Accordingly, in this analysis, the optical-admittance calculation is first performed from the bottom to the top layer ($Y_j \rightarrow Y_0$) using Eq. (1) to deduce R_{flat} from Eq. (2). By applying this R_{flat}, the layer absorptance is determined from the top to bottom layer ($A_1 \rightarrow A_j$) using Eqs. (3) and (4). Once the absorptance in each layer is known, the EQE spectrum can then be simulated assuming 100% collection efficiency for the generated carriers in the CIGS layer. Finally, the J_{SC} of the solar cell is calculated as

$$J_{\text{SC}} = \frac{e\lambda}{2\pi\hbar c}\int A(\lambda)F(\lambda)d\lambda, \tag{5}$$

where e and c are the electron charge and the speed of light, respectively. In Eq. (5), $A(\lambda)$ shows the absorptance (EQE) spectrum of the CIGS layer [i.e., $A(\lambda) = \text{EQE}(\lambda)$], whereas $F(\lambda)$ indicates the solar irradiance in units of W cm^{-2} nm^{-1} under AM1.5G illumination.

In nonuniform structures with rough surfaces, on the other hand, strong light scattering occurs when the size of the surface texture becomes comparable to the wavelength of the incident light [see Fig. 2(b)]. Under this condition, the transmission angle in the layered structure shows a broad distribution [57], which requires a quite complex calculation for the evaluation of $A(\lambda)$. Nevertheless, if we apply the experimental reflectance obtained directly from actual device structures (R_{ex}), the total light absorptance in the solar cells can be obtained quite easily as $\sum A_j = 1 - R_{\text{ex}}$. Since R_{ex} includes all the possible effects of light scattering in the solar cell, this procedure allows for an accurate and simple estimation of $\sum A_j$. Unfortunately, even in this case, the calculation of A_j from $\sum A_j$ is not straightforward because of the complexity of the solar-cell

structure. As shown in Fig. 2(b), however, even when the transmitted light is scattered, the ratio of the optical pass lengths within the solar-cell component layers may not differ significantly from the case of a flat structure if the angular distribution of the scattered light is small. Thus, we have solved the complicated problem of light scattering by calculating A_j while assuming a perfectly flat structure, whereas $\sum A_j$ itself is estimated from $(1 - R_{ex})$. This analysis can be conducted easily by simply replacing R_{flat} in Eq. (4) with R_{ex}. In other words, our approach assumes that there is no change in the internal QE spectra between perfectly flat and textured structures.

For the EQE analysis of the CIGS solar cells, we construct an optical model consisting of the $MgF_2/ZnO:Al/ZnO/CdS/CIGS/MoSe_2/Mo$ structure, as shown in Fig. 2(c). The thicknesses of the solar-cell component layers are determined from direct observation of the TEM measurements in Fig. 1, and the layer thicknesses used in the EQE calculation are shown in Fig. 2(c). For the ZnO:Al/ZnO two-layer structure, however, determination of each layer thickness from the TEM images is difficult, as the ZnO grain growth is continuous. Thus, we obtain the thickness of the nondoped-ZnO layer from a separate experiment (50 nm), and the ZnO:Al thickness is estimated by subtracting the ZnO layer thickness from the total ZnO:Al/ZnO thickness observed in the TEM images. In the actual EQE simulation, a minor adjustment of the CdS layer thickness is made within the uncertainty of the TEM thickness measurement (<5%) to obtain a better EQE fitting.

B. Optical constants of component layers

Figure 3 summarizes the optical constants employed for the EQE simulation [58]. The (n, k) results for the $CuIn_{1-x}Ga_xSe_2$ layers with different Ga compositions $[x = Ga/(In + Ga)]$ are obtained from the spectroscopic ellipsometry (SE) analysis reported previously [48]. The Cu composition $y = Cu/(In + Ga)$ of these layers is approximately 0.90. In Fig. 3(a), the onset of $k > 0$ roughly corresponds to the band gap E_g and the critical point E_0. As x increases, the k spectrum shifts toward higher energies with no significant variation in the spectral shape. Thus, the corresponding α spectrum (i.e., $\alpha = 4\pi k/\lambda$) also slides toward higher energies with increasing x [48]. For the calculation of the CIGS optical constants with different x values, we employ an energy-shift model [59] in which the dielectric function of an arbitrary composition is "synthesized" from a set of known dielectric functions by adjusting the energy spacing of the spectra so that the optical transition (critical point) energies match with those of the target composition.

In the actual calculation, we use the CIGS dielectric functions corresponding to the optical constants in Fig. 3(a), and the CIGS dielectric function of an intermediate composition of $x = 0.20$, for example, is obtained

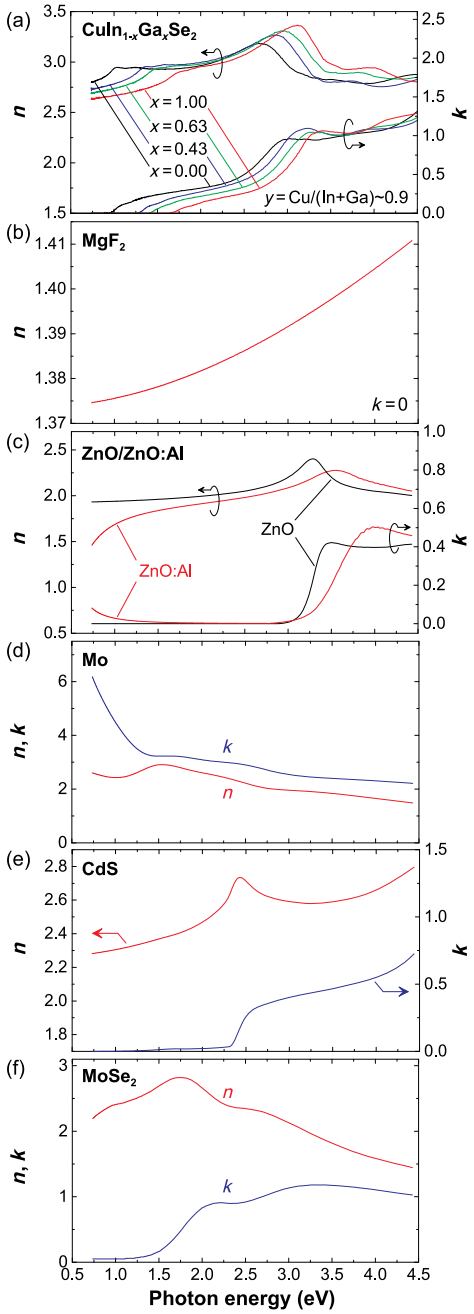

FIG. 3. Optical constants employed for the EQE simulation [58]: (a) CIGS with different $x = Ga/(In + Ga)$ values, (b) MgF_2, (c) nondoped ZnO and ZnO:Al, (d) Mo, (e) CdS, and (f) $MoSe_2$. The numerical values for (f) and (e) are taken from Refs. [15] and [60], respectively.

from two dielectric functions of $x = 0.00$ and 0.43 by taking the shift of the critical point energies with x into account. The variation of $E_g(E_0)$ with x and y is expressed by $E_g = (1.00 + 0.71\,x) + 0.34(0.90 - y)$ eV [48]. Here, the term for y shows the effect of the Cu $3d$ and Se $4p$ interaction on the E_g variation [48,61,62]. On the other hand, the transition peak in CIS ($x = 0.00$) at a photon energy of $E \sim 3.0$ eV [the $E_1(A)$ critical point] shifts with

$E_1(A) = 2.94 + 0.39x$ eV [48]. Thus, from the predetermined critical point energies of CIGS, the optical constants can be obtained using the energy-shift model.

In our CIGS optical database, the amplitude change of the dielectric function with y has also been modeled. In particular, we previously reported that, as y decreases, the amplitude of the dielectric function also reduces with no apparent shift of the peak transition energies, except for E_0 [48]. Thus, the variation of CIGS optical constants with y can be modeled simply as the weighted average of the two spectra with smaller and larger y values. For the calculation of the CIGS solar cell in Fig. 1, $y = 0.91$ evaluated from inductively coupled plasma mass spectroscopy (ICP MS) is used. The details of the CIGS optical database will be reported elsewhere.

The optical constants of the MgF_2 in Fig. 3(b), the ZnO:Al and ZnO layers in Fig. 3(c), and the Mo layer in Fig. 3(d) are extracted from individual single layers formed on flat substrates using standard SE analyses [63]. For these analyses, the MgF_2, ZnO:Al, and ZnO layers are prepared on crystalline Si(c-Si) substrates covered with SiO_2 native oxides (approximately 2 nm) using deposition conditions identical to those in the solar-cell preparation, while a soda-lime glass substrate is used for the Mo layer fabrication. The n spectrum of the MgF_2 in Fig. 3(b) is determined from the Cauchy model [63] $n(\lambda) = A + B/\lambda^2$ [$k(\lambda) = 0$] using the optical model of an MgF_2 (bulk layer)/SiO_2/c-Si substrate structure. The parameter values of the model are $A = 1.374$ and $B = 2.94 \times 10^3$ nm^2.

The optical constants of the ZnO:Al and ZnO layers are extracted using a procedure established previously that employs the mathematical inversion [64]. The (n, k) spectra shown in Fig. 3(c) are obtained from the ZnO samples with layer thicknesses of 100 nm (ZnO:Al) and 50 nm (nondoped ZnO). In Fig. 3(c), the light absorption at $E > 3.0$ eV shows the interband transition in the ZnO and ZnO:Al layers. The absorption edge shifts toward higher energy in the ZnO:Al, compared with the nondoped ZnO, since a high carrier concentration of 10^{20} cm^{-3} in the ZnO:Al causes the Fermi level to shift deep into the conduction band, which, in turn, increases the interband transition energy (a Burstein-Moss shift) [64,65]. In the ZnO:Al, the k values also increase at lower energies because of the free carrier absorption [63], and the EQE spectrum is influenced strongly by the presence of the free carrier absorption. Since the free carrier absorption changes with the optical carrier concentration (N_{opt}) and the optical mobility (μ_{opt}) in doped transparent conductive oxide (TCO) layers [64], appropriate values should be used for these parameters.

As reported previously [64,66,67], the free carrier absorption in doped-ZnO layers can be expressed completely by the Drude model. The dielectric function of the Drude model is given by $\varepsilon_{Drude}(E) = -A_D/(E^2 - i\Gamma_D E)$, where

$$A_D = \frac{\hbar^2 e^2 N_{opt}}{\varepsilon_0 m^*}, \tag{6}$$

$$\Gamma_D = \frac{\hbar e}{m^* \mu_{opt}} \tag{7}$$

Here, ε_0 and m^* are the free-space permittivity and effective mass, respectively. As confirmed from Eqs. (6) and (7), A_D is proportional to N_{opt}, whereas Γ_D is inversely proportional to μ_{opt}. In the TCO layers, however, m^* changes with N_{opt} because of the degeneracy and nonparabolicity of the TCO conduction band [64,68,69]. In this case, m^* of ZnO is given as follows [64]:

$$m^* = (0.280 + 0.010 \times 10^{-20} N_{opt}) m_0. \tag{8}$$

As a result, when the Drude model is applied, the free carrier absorption is determined from the two values of (A_D, Γ_D) or (N_{opt}, μ_{opt}). It should be noted that N_{opt} shows quite good agreement with the carrier concentration determined by the Hall measurement [64]. Nevertheless, μ_{opt} generally has a much higher value than the mobility obtained from the Hall measurement (μ_{Hall}), as μ_{opt} does not include the effect of grain-boundary scattering [66,67]. Thus, if the value of μ_{Hall} is applied for the calculation, the free carrier absorption in the ZnO:Al layer will be overestimated, since the free carrier absorption increases with Γ_D.

In the actual EQE analyses, the parameter value of $A_D(N_{opt})$ is adjusted slightly so that the EQE fitting improves. In this case, the ZnO:Al dielectric function in the low-energy region of $E < 3.0$ eV is parametrized by combining the Tauc-Lorentz (TL) model [70] with the Drude model, as reported previously [64,71]. For the ZnO:Al layer in Fig. 3(c), the parameter values of the TL model are $A_{TL} = 110.92$ eV, $E_g = 2.76$ eV, $E_0 = 7$ eV, $C = 12$ eV, and $\varepsilon_1(\infty) = 1$, whereas the Drude parameters are $A_D = 0.85$ eV and $\Gamma_D = 0.114$ eV, which correspond to $N_{opt} = 1.8 \times 10^{20}$ cm^{-3} and $\mu_{opt} = 34$ cm^2/V s, respectively. In general, N_{opt} in doped-ZnO layers increases strongly with the layer thickness [67]. In fact, when the ZnO:Al layer thickness on the SiO_2/c-Si substrate increases from 100 nm [the sample in Fig. 3(c)] to 300 nm, the multilayer analysis of the free carrier absorption [67] shows an increase in N_{opt} from 1.8×10^{20} cm^{-3} to 2.7×10^{20} cm^{-3}. In our simulation, however, the single ZnO:Al layer is employed in the optical model to simplify the analysis [see Fig. 2(c)]. For this layer, a fixed Γ_D value of 0.114 eV determined from the ZnO:Al layer (100 nm) on the flat substrate is used, as μ_{opt} is independent of the thickness [67], and only the A_D value is changed slightly to express the variation of the free carrier absorption in the ZnO:Al layer incorporated into the solar cells.

The Mo optical constants in Fig. 3(d) are obtained from the SE analysis, assuming a surface roughness and Mo bulk

layer structure. In this analysis, the surface roughness layer thickness (d_s) and void volume fraction (f_{void}) in the Mo roughness layer are first estimated using a reported Mo dielectric function [15] and applying the Bruggeman effective-medium approximation [63]. By using the $d_s = 54.3$ nm and $f_{\text{void}} = 0.31$ values obtained from this analysis, the dielectric function of the Mo layer is then extracted from the (ψ, Δ) ellipsometry spectra using the mathematical inversion. As confirmed from Fig. 3(d), Mo exhibits metallic optical properties characterized by high k values.

The dielectric functions obtained from our analyses reproduce results previously reported for MgF_2 [72,73], ZnO [64], ZnO:Al [64], and Mo [15,74]. For the CdS layer, a dielectric function obtained from sputtering deposition [60] is used for the EQE calculation, as the preparation of CdS layers with small roughness was difficult in the CBD process. The CdS optical constants shown in Fig. 3(e) are obtained by fitting the reported CdS dielectric function [60] using the Tauc-Lorentz model. We also perform the SE fitting analysis of the CdS layer prepared by the CBD process using the optical constants in Fig. 3(e) and confirm a reasonably good fitting. Thus, the optical properties of the sputtered CdS layer are similar to the CBD-processed CdS layer. As shown in Fig. 3(e), the CdS layer shows strong light absorption above $E_g = 2.39$ eV. The k spectrum of the CdS layer also indicates the presence of light absorption below E_g, probably induced by the imperfection of the CdS polycrystalline structure. In addition, the (n, k) spectra of $MoSe_2$ shown in Fig. 3(f) represent the data reported by Richter *et al.* [15] as the preparation of sufficiently thick $MoSe_2$ layers is not established in this work. Basically, $MoSe_2$ is a semiconductor with $E_g \sim 1.4$ eV [56], although weak light absorption persists below E_g.

IV. RESULTS

A. EQE calculation for CIGS solar cells

To justify our EQE analysis procedure based on the extended optical-admittance method described in Sec. III A, we calculate the EQE spectrum of the CIGS solar cell fabricated by the three-stage process. Figure 4 shows the depth profiles for x and y in the 1.8-μm-thick CIGS layer incorporated into the solar cell shown in Fig. 1. In this figure, (x, y) values for the depth from the CdS/CIGS interface (d) are indicated. The compositional profiles are measured using secondary ion mass spectroscopy (SIMS), and the absolute compositions are calibrated from ICP MS. For the ICP MS measurement, the CIGS sample is dissolved by an acid solution. In Fig. 4, the open circles denote the measured results, and the solid lines indicate the fitting results. The depth profile for x is fitted assuming an asymmetric double-Gaussian profile expressed by

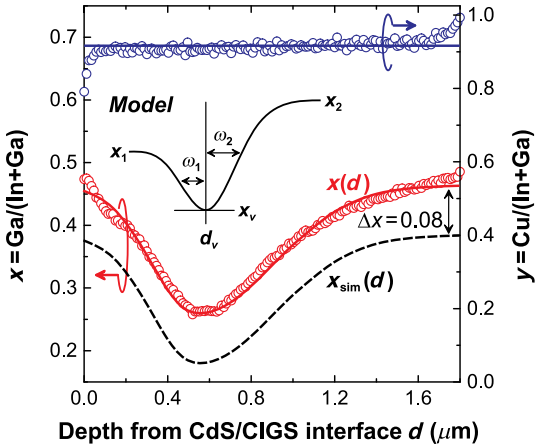

FIG. 4. Depth profiles for x and y in the 1.8-μm-thick CIGS layer measured by SIMS. In this figure, the open circles denote the measured data, and the solid lines indicate the fitting results. The solid line denoted as $x(d)$ shows the asymmetric double-Gaussian function, and the dotted line denoted as $x_{\text{sim}}(d)$ represents the shifted profile [$x_{\text{sim}}(d) = x(d) - 0.08$] used in the optical simulation.

$$x(d) = \begin{cases} x_1 - (x_1 - x_v)\exp\{-[(d-d_v)/\omega_1]^2\} & (d \le d_v) \\ x_2 - (x_2 - x_v)\exp\{-[(d-d_v)/\omega_2]^2\} & (d > d_v) \end{cases}, \tag{9}$$

where x_1 and x_2 are the saturation values at $d = 0$ and 1800 nm, respectively. The x_v and d_v denote x and d at the valley position of the V-shaped Ga profile, respectively. In addition, the $\omega_{1,2}$ values are the broadening parameters for the Gaussian profile, which are switched at d_v. In our optical simulation, however, the x values in Fig. 4 are reduced slightly with a constant value of $\Delta x = 8$ at. % [i.e., $x_{\text{sim}}(d) = x(d) - \Delta x$], to obtain a good fitting to the experimental EQE data. The profile parameters for $x_{\text{sim}}(d)$ are $x_1 = x_2 = 0.38$, $x_v = 0.18$, $d_v = 540$ nm, $\omega_1 = 308$ nm, and $\omega_2 = 527$ nm. For the Cu profile, we assumed a constant value of $y = 0.91$, although the measured y values reduce near the CdS interface ($d < 50$ nm).

Figure 5 shows the EQE and reflectance spectra of the CIGS solar cell together with the calculation results obtained from (a) the optical-admittance method and (b) the simulation method developed in this work. In the EQE calculation, the CIGS layer is divided into 500 sublayers, and the x value in each sublayer is obtained from $x_{\text{sim}}(d)$ shown in Fig. 4. In Fig. 5(a), the open circles denote the experimental EQE spectrum obtained from the actual CIGS solar cell (QE_{ex}), and the corresponding reflectance spectrum of the solar cell (R_{ex}) is also shown. The R_{flat} in Fig. 5 shows the reflectance spectrum calculated from Eq. (2) using the perfectly flat optical model in Fig. 2(c) and the optical constants of Fig. 3. It can be seen that the calculated R_{flat} is rather similar to R_{ex}. However, the absolute values of R_{flat} are larger than those of R_{ex}.

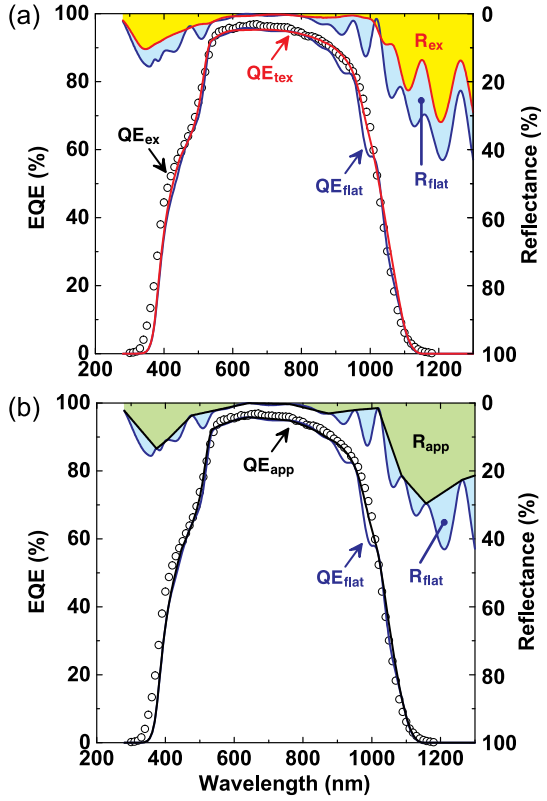

FIG. 5. Experimental EQE spectrum of the CIGS solar cell consisting of MgF_2 (130 nm)/ZnO:Al (360 nm)/ZnO (50 nm)/CdS (45 nm)/CIGS (1800 nm)/$MoSe_2$ (10 nm)/Mo (QE_{ex}, open circles) together with the calculated EQE results (solid lines) obtained from (a) the optical-admittance calculation assuming a flat structure (QE_{flat}) and a textured structure (QE_{tex}) and (b) the simulation method developed in this work (QE_{app}). In this figure, the reflectance spectra are also shown; R_{ex} indicates the experimental reflectance spectrum, whereas R_{flat} and R_{app} show the spectra obtained from the flat optical model and the linear approximation under the antireflection condition, respectively.

This result confirms the fact that light scattering due to the submicron natural texture of the CIGS layer effectively suppresses the front light reflection particularly by eliminating the interference fringes. Thus, the difference between R_{ex} and R_{flat} can be considered as an actual texture effect of the whole CIGS solar cell.

The EQE spectrum denoted as QE_{flat} in Fig. 5(a) indicates the results obtained from Eq. (4) using R_{flat} as a reflectance spectrum. Although QE_{flat} agrees rather well with QE_{ex}, QE_{flat} deviates largely from QE_{ex} in the wavelength range of $\lambda = 800$–1100 nm because of the appearance of the interference pattern induced by the assumed flat structure. Thus, if we remove the effect of the interference, QE_{flat} is expected to show a better fitting to QE_{ex}. Accordingly, we perform the optical simulation by applying R_{ex} to Eq. (4), instead of R_{flat}, to incorporate the effect of the front light scattering by the CIGS natural texture, as described in Sec. III A. In this calculation, the reflectance difference corresponding to $\Delta R = R_{flat} - R_{ex}$ is also absorbed within the CIGS solar cell, and this extra light absorption is distributed among the component layers assuming a flat structure. In Fig. 5(a), QE_{tex} shows the calculation results obtained using R_{ex} in Eq. (4). By this procedure, the interference effect in QE_{flat} is suppressed almost completely, and QE_{tex} shows excellent agreement with QE_{ex} in the wide spectral range. In the region of $\lambda < 600$ nm, however, QE_{flat} and QE_{tex} indicate a similar optical response, as strong light absorption occurs in the ZnO:Al/CdS front layers.

In the above calculation scheme, R_{ex} is always necessary, which restricts the use of this method. Nevertheless, R_{ex} can be approximated by linearly connecting the minimum positions of the inference pattern that appears in R_{flat}, as shown in Fig. 5(b). The minimum positions in R_{flat} can be determined by selecting λ values where the condition $dR_{flat}(\lambda)/d\lambda = 0$ is satisfied. When this approximated reflectance spectrum (R_{app}) is employed in the calculation of Eq. (4), we obtain an EQE spectrum (QE_{app}) quite similar to QE_{tex}. In a multilayer system, the minimum position of the interference pattern basically represents the antireflection condition, in which the multiply reflected beams generated within the layered structure are out of phase. In the R_{app} calculation, therefore, the antireflection condition is superimposed on the result of R_{flat} to simulate the effect of the elimination of the interference fringe by the textured structure. This approach liberates the restriction of the EQE calculation and extends the EQE simulation to arbitrary compositional profiles and device structures. In the calculation of R_{app} from R_{flat}, however, when the background reflectance changes, it sometimes becomes difficult to find the minimum interference positions in R_{flat}. This difficulty occurs particularly in the region where the interference effect is weak and the condition $dR_{flat}(\lambda)/d\lambda = 0$ is not satisfied. Thus, in the developed simulation method, a slight ambiguity remains for the selection of the minimum points in the weak interference regime.

From the EQE spectra in Fig. 5, J_{SC} is calculated using Eq. (5). The J_{SC} values obtained are 34.0 mA/cm^2 (QE_{tex}), 33.8 mA/cm^2 (QE_{app}), and 33.4 mA/cm^2 (QE_{flat}) for the experimental value of 34.2 mA/cm^2 (QE_{ex}). Thus, the effect of the texture on J_{SC} is small in our solar cell ($QE_{tex} - QE_{flat} = 0.6$ mA/cm^2). The light scattering caused by the rough structures is essentially determined by the size of the textures relative to the wavelength of the incident light [57]. As confirmed from the TEM image of the CIGS solar cell in Fig. 1(a), the size of the CIGS natural texture is approximately 100 nm and is relatively small, compared with λ in the EQE spectra ($\lambda = 300$–1200 nm). Accordingly, the light scattering in the CIGS solar cell is rather weak, especially in the longer-wavelength region, and the optical pass length within the solar-cell component layers can be approximated quite well by assuming a flat

optical model. The above results indicate clearly that the major impact of the CIGS texture on the EQE spectrum is the elimination of the optical interference in the solar cell. In addition, the light scattering within the component layers is also expected to be quite weak. Since light scattering occurs when the surface or interface has a large contrast in N, the scattering effect inside the thin layers can be neglected, unless there are large void-related structures with dimensions comparable to the wavelength of the incident light.

In the EQE analysis of Fig. 5, on the other hand, the x value in the CIGS layer is modified using $\Delta x = 0.08$ in Fig. 4 to obtain a good EQE fitting. It should be stressed that the longer-wavelength response is essentially determined by the minimum E_g ($E_{g,\mathrm{min}}$) that corresponds to the lowest x in the Ga-compositional profile (i.e., x_v in Fig. 4) [7,35] and that no strong light absorption occurs below $E_{g,\mathrm{min}}$ in the CIGS solar cells. In the case of Fig. 5, the EQE in the longer-wavelength region reduces sharply with the intercept of $\lambda = 1100$ nm, which is equivalent to $E_{g,\mathrm{min}} \sim 1.13$ eV. In our CIGS optical database, however, this $E_{g,\mathrm{min}}$ is not consistent with $x_v = 0.26$ obtained from the ICP MS-SIMS compositional analysis of the solar cell. In particular, when the x_v value used in the calculation is inappropriate, the simulated EQE spectrum deviates largely from $\mathrm{QE_{ex}}$ in the longer-wavelength region, as shown in the simulation results of Fig. 10(e). In our EQE simulation, therefore, the values of the whole $x(d)$ profile are reduced using Δx as a free parameter.

On the other hand, since the submicron texture is present in the CIGS solar cell, it is possible that the $x(d)$ profile in Fig. 4 is broadened in the SIMS analysis, which, in turn, increases the x_v value. To find the influence of the depth-profile broadening, we apply a sharper x profile by reducing both $\omega_{1,2}$ and x_v, while keeping the integrated $x(d)$ value unchanged. In this case, however, no satisfactory fitting is obtained, and the EQE at around $\lambda = 950$ nm is seriously underestimated. The x values in our CIGS optical database were originally determined by electron-probe microanalysis (EPMA). Unfortunately, this method is rather difficult to apply for the CIGS layer fabricated by the three-stage process because of the limited depth sensitivity. Based on the above results, we suggest that the inconsistency of x between the ICP MS-SIMS analysis and the EQE simulation in Figs. 4 and 5 arises from the calibration error between the ICP MS and EPMA measurements.

In the EQE simulation of Fig. 5, a minor adjustment is also made for A_D of the ZnO:Al, in addition to Δx. It will be shown in Figs. 6 and 11 that the maximum EQE at $\lambda = 800$ nm is determined almost completely by the free carrier absorption in the ZnO:Al and, to perform an accurate analysis, A_D needs to be changed slightly from that determined from the single ZnO:Al layer on the flat substrate. Specifically, when we apply $N_{\mathrm{opt}}=2.4\times10^{20}\mathrm{cm}^{-3}$ obtained as an average value of the 300-nm-thick ZnO:Al layer on the flat substrate, a nonphysical value for $\mathrm{QE_{tex}}$, which is lower than $\mathrm{QE_{ex}}$, is obtained. Thus, in our simulation, $N_{\mathrm{opt}}(A_D)$ is reduced slightly to 1.8×10^{20} cm^{-3} (0.85 eV), which is equivalent to N_{opt} of the ZnO:Al in Fig. 3(c). This implies the run-to-run variation or the substrate dependence of N_{opt} in the ZnO:Al layer.

All the other simulation parameters concerning the device structure and optical constants are determined unambiguously from the independent TEM and SE analyses. Accordingly, the excellent agreement between $\mathrm{QE_{tex}}$ and $\mathrm{QE_{ex}}$ in Fig. 5 strongly supports the validity of our EQE simulation method. This result also confirms that $\mathrm{QE_{ex}}$ of the CIGS solar cell can be reproduced even when we use the recently reported low α values for CIGS-based layers [48] ($\alpha = 6.6 \times 10^4$ cm^{-1} at 2.0 eV for CIS), which are far smaller than those widely cited [52] ($\alpha = 1.7 \times 10^5$ cm^{-1} at 2.0 eV for CIS). Furthermore, the good agreement between $\mathrm{QE_{ex}}$ and $\mathrm{QE_{tex}}$ indicates clearly that the carrier collection efficiency in the CIGS light-absorber layer is almost 100% with little carrier recombination loss. In previous simulation studies [12,15], very high carrier collection efficiencies in CIGS light-absorber layers have also been reported. The above results provide direct evidence that the carrier recombination at CIGS grain boundaries is negligible in CIGS solar cells. It is widely known that Cu-deficient structures (ordered vacancy compounds) created near the CIGS surface [1,75] induce a type-II band alignment in the surface region [75,76], which suppresses the carrier recombination quite effectively. A theoretical study indicates that the formation of the Cu-poor grain interface is also beneficial for carrier collection in the grain-boundary region [77].

The result of Fig. 5 demonstrates that highly accurate EQE simulations can be performed by applying R_{ex} to the optical-admittance calculation. We confirm that good fittings can also be obtained in other CIGS solar cells. In the developed method, modeling of the rough interface structure is not necessary, and the EQE spectra can be calculated quite easily at high speed. Moreover, the good fitting without the introduction of interface layers in the optical model shows that the antireflection effect by interface mixing is quite weak in the CIGS solar cells. Quite fortunately, the EQE simulation of CIGS-based solar cells can be performed rather easily by utilizing the antireflection condition. From the developed simulation technique, the EQE spectra of a wide variety of CIGS solar-cell structures can be calculated with sufficient accuracy, as described in Sec. IV C.

B. Optical gain and loss in a CIGS solar cell

Figure 6 shows the absorptance spectra of the solar-cell component layers obtained from the EQE analysis of Fig. 5(a). In this figure, the R_{ex} of the solar cell is also

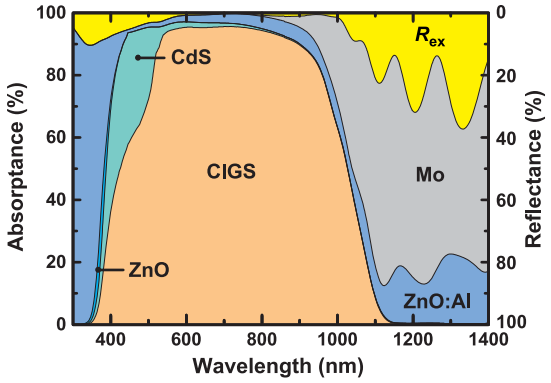

FIG. 6. Absorptance spectra of the component layers in the CIGS solar cell. In this figure, the R_{ex} of the solar-cell structure is also indicated.

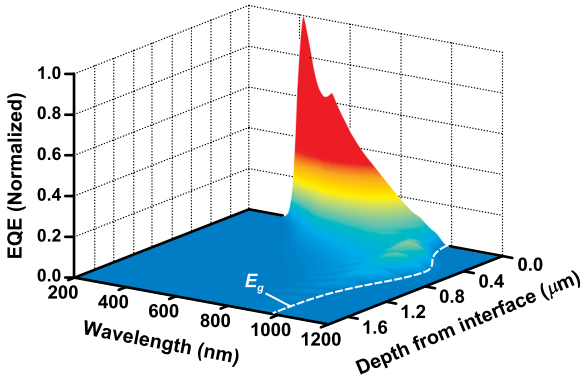

FIG. 7. Normalized partial EQE calculated for different depths from the CdS/CIGS interface and wavelengths. The dotted line represents E_g of the CIGS at each depth determined from $x_{sim}(d)$ and y in Fig. 4.

shown. The absorptance spectrum for the CIGS layer is identical to the QE_{tex} spectrum in Fig. 5(a), as 100% carrier collection is assumed. The light absorption in the nondoped ZnO and $MoSe_2$ (not shown) is negligible because of the small layer thicknesses and low α values of these layers.

The large light absorption in the ZnO:Al layer at $\lambda < 445$ nm is caused by the interband transition, whereas the continuous light absorption in the visible-infrared regime shows the contribution of the free carrier absorption. Thus, the free carrier absorption in the TCO layer suppresses the overall EQE, and the maximum EQE at $\lambda = 800$ nm is determined preliminarily by the free carrier absorption. At $\lambda = 320$–500 nm in Fig. 5, on the other hand, QE_{tex} exhibits slightly lower values compared with QE_{ex}. As mentioned earlier, the effective E_g of the doped TCO layers increases with increasing N_{opt} due to the Burstein-Moss shift. However, this effect is not modeled in our simulation, and the EQE fitting can be improved by shifting the onset of the interband transition in the ZnO:Al layer toward higher energy (i.e., lower wavelength).

As reported previously [11,22,23], the presence of the CdS layer leads to the strong EQE reduction at $\lambda = 400$–540 nm due to the direct optical transition in the CdS at $E \geq 2.3$ eV [see Fig. 3(e)]. The result of Fig. 6 also reveals that rather strong light absorption occurs in the metallic Mo layer and that the EQE response in the longer-wavelength region is essentially limited by the parasitic light absorption in the Mo layer.

Figure 7 shows the normalized partial EQE calculated for different depths from the CdS/CIGS interface (i.e., d in Fig. 4) and wavelengths. If the partial EQE spectrum obtained at different d values is integrated, the absorptance spectrum shown in Fig. 6 can be obtained. The partial EQE is quite high at $d \sim 0$ μm and exhibits a rapid decay versus d due to the strong light absorption in the CIGS layer. The partial EQE spectrum at $d \sim 0$ μm indicates the oscillation pattern in the region of $\lambda = 400$–600 nm because of the interference effect induced by the CdS layer. The optical interference that occurs within the CIGS layer also modulates the partial EQE in the region of $d > 0.4$ μm with $\lambda = 800$–1100 nm. The dotted line in Fig. 7 represents E_g of the CIGS at each depth determined from $x_{sim}(d)$ and $y = 0.91$. In particular, at $d_v = 0.54$ μm, E_g shows the lowest value of 1.12 eV $(x_v = 0.18)$, and the upper limit for the light absorption extends into the longer-wavelength region.

Figure 8 shows (a) the partial absorptance in the ZnO:Al/ZnO/CdS/CIGS solar-cell structure obtained at different d and λ values, (b) the integrated J_{SC} for d, and (c) the integrated J_{SC} for λ. The partial absorptance of the CIGS in Fig. 8(a) corresponds to the partial EQE of Fig. 7. When the partial absorptance spectra for the ZnO:Al, ZnO, and CdS layers are integrated, those in Fig. 6 can be obtained. In Fig. 8(a), the absorptance values are normalized by the maximum values obtained in each layer. The dotted lines in Fig. 8(a) indicate E_g in each layer. As shown in Fig. 8(a), the strong light absorption occurs below λ, which corresponds to E_g of each component layer, and the onset of the absorption shifts toward the longer wavelength as E_g reduces gradually from the top ZnO:Al to the bottom CIGS layer. Because of the light absorption in the upper layer, the partial absorptance in the short-wavelength region is limited by the E_g of the upper layer. In the case of the nondoped-ZnO layer, the E_g of this layer is slightly smaller than that of the ZnO:Al because of the Burstein-Moss shift, and the light absorption occurs in a quite narrow region. The result of Fig. 8(a) confirms that the light absorption in the CdS layer reduces the partial absorptance of the CIGS layer at $\lambda = 400$–540 nm. In Fig. 8(a), the interference effects are visible within the ZnO:Al (the free carrier absorption regime at $\lambda > 750$ nm) and CIGS layers.

In Fig. 8(b), the partial absorptance in the CIGS layer is integrated toward the depth to deduce the contribution of the absorptance at each depth for J_{SC}. The light absorption in the CIGS layer occurs predominantly at $d < 600$ nm, and J_{SC} increases rapidly in this thickness region. In

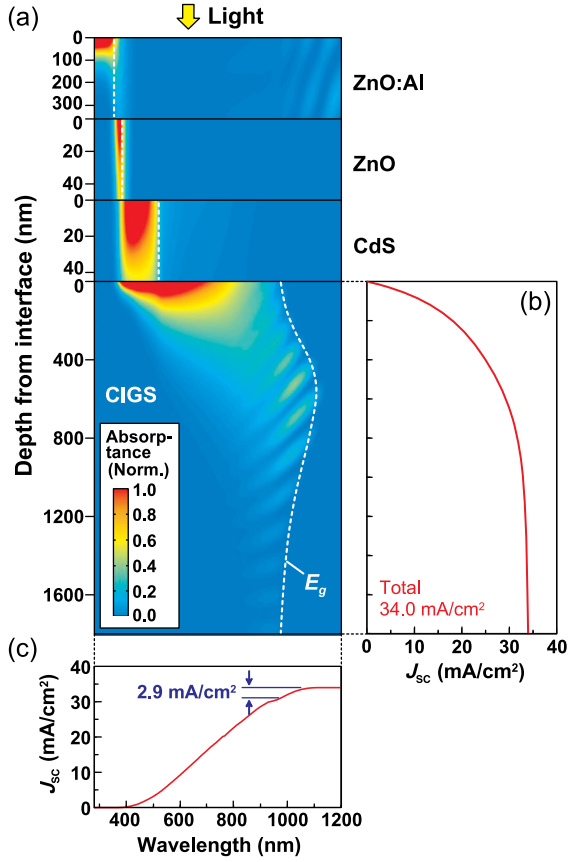

FIG. 8. (a) Partial absorptance in the ZnO : Al/ZnO/CdS/CIGS solar-cell structure obtained at different depths from each interface and wavelengths, (b) the integrated J_{SC} for d, and (c) the integrated J_{SC} for λ. The value of the partial absorptance is normalized by the maximum in each layer, and the absorptance of the CIGS in (a) corresponds to the partial EQE of Fig. 7. The dotted line represents E_g in each layer.

contrast, the increase in J_{SC} is almost negligible in the 1-μm-thick CIGS bottom layer. This result is not surprising since the α value at $\lambda = 600$ nm is 5.8×10^4 cm^{-1} for $x = 0.43$ in Fig. 3(a), and the resulting penetration depth ($d_p = 1/\alpha$) is only 170 nm. This high α value in the CIGS layer explains the quite rapid decay of the absorptance over d. It should be noted that, if we assume a higher α of 1.7×10^5 cm^{-1}, d_p reduces further to 60 nm. In Fig. 8(c), the contribution of each λ for J_{SC} is shown. In our CIGS solar cell, the gain of J_{SC} by the light absorption below E_g of the CIGS bottom layer ($\lambda \geq 979$ nm) is 2.9 mA/cm^2. The effect of the lowest x in the CIGS solar cell on J_{SC} will be discussed in Sec. V A in more detail.

Figure 9 summarizes the optical gain and loss in the CIGS solar cell. These values are estimated from the absorptance spectra shown in Fig. 6. When $E_{g,\min}$ in the CIGS layer is 1.12 eV ($x_v = 0.18$), the maximum J_{SC} value attainable under the AM1.5G condition is 43.72 mA/cm^2. As indicated in the figure, the reflection loss calculated from R_{ex} is 1.20 mA/cm^2, whereas the total absorption loss is 8.52 mA/cm^2. Major parasitic light absorption occurs in the ZnO:Al, CdS, and Mo layers with optical losses of 2.66, 2.51, and 3.22 mA/cm^2, respectively. For the ZnO:Al, the absorption loss due to the free carrier absorption (1.68 mA/cm^2) is larger than that caused by the interband transition (0.98 mA/cm^2), as the number of photons is reduced at higher energies [78]. Although the CdS layer is quite thin (approximately 50 nm), the J_{SC} loss attributed to this layer is quite large, since the CdS has relatively large $k(\alpha)$ values. Among the solar-cell component layers, the Mo layer shows the largest parasitic absorption with a J_{SC} loss exceeding 3 mA/cm^2. On the other hand, the optical losses in the nondoped-ZnO and $MoSe_2$ layers are quite small.

As shown in Fig. 9, the total optical gain in the CIGS layer is 34.00 mA/cm^2. When the optical gain is divided into the three sublayers with an equal thickness of 600 nm, J_{SC} generated in the top sublayer accounts for 86% of the total gain, while photocarrier generation in the bottom sublayer accounts for only 2%.

C. EQE simulation

To investigate the effect of the CIGS compositional profile and the layer thickness on the EQE spectrum, we perform an EQE simulation using the QE_{app} calculation procedure shown in Fig. 5(b). Figure 10 shows the results of the EQE simulation for different $x_{sim}(d)$ profiles obtained with variation of (a) ω_2, (b) x_v, and (c) d_v, and the EQE spectra calculated from these $x_{sim}(d)$ profiles are shown in Figs. 10(d), 10(e), and 10(f), respectively. These simulations are performed based on the structure of our CIGS solar cell. Specifically, the thicknesses of the component layers are fixed to those of the CIGS solar cell indicated in Fig. 2(c). For the calculation of the $x_{sim}(d)$

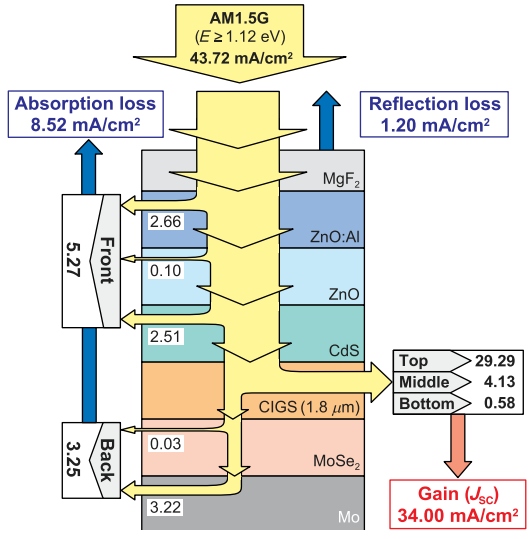

FIG. 9. Optical gain and loss in the CIGS solar cell. The numerical values indicated in the figure show the corresponding current densities in units of mA/cm^2.

profiles, the parameters extracted from $x_{\mathrm{sim}}(d)$ in Fig. 4 are employed as a basis and only the profile parameters denoted in Figs. 10(a)–10(c) are changed. In the case of Fig. 10(b), for example, only one parameter (x_v) is varied from 0.00 to 0.38, whereas the values of the other parameters (i.e., x_1, x_2, d_v, ω_1, ω_2) are identical to those of $x_{\mathrm{sim}}(d)$ in Fig. 4.

In the simulation of Fig. 10(a), we employ a fixed ratio of $\omega_1/\omega_2 = 0.58$ obtained experimentally, and the ω_2 value is changed from 300 to 700 nm. Quite interestingly, the variation of ω_2 from 300 to 700 nm does not lead to a significant change in the EQE response. As mentioned earlier, the long-wavelength limit for the EQE is governed by x_v in the profile. In the case of Fig. 10(d), x_v is constant, and the EQE limit ($\lambda = 1100$ nm) does not change. On the other hand, since d_p in the CIGS layer is of the order of 200 nm because of the relatively high α values, the effective absorber thickness of approximately 200 nm for $x_v \sim 0.2$ is sufficient to gain enough EQE at $\lambda \sim 1000$ nm. Accordingly, J_{SC} in Fig. 10(d) changes only moderately from 32.81 mA/cm^2 ($\omega_2 = 300$ nm) to 34.45 mA/cm^2 ($\omega_2 = 700$ nm).

When x_v is varied, however, the EQE changes drastically, as shown in Fig. 10(e). In this case, the EQE response extends largely toward longer wavelengths as x_v is reduced. As a result, J_{SC} of the solar cell increases from 30.38 mA/cm^2 ($x_v = 0.38$) to 37.33 mA/cm^2 ($x_v = 0.00$). The simulation results of Fig. 10(f) show clearly that the position of d_v in the profile has almost no effect on the EQE spectrum. As confirmed from Fig. 8, even when d_v is located further from the CdS/CIGS interface, no significant light absorption occurs in the wavelength region below E_g of the upper CIGS layer. Thus, the light in the wavelength region corresponding to $E_g(x_v) \le E < E_g(x_1)$ is simply transmitted though the upper layer and is absorbed near d_v, independent of the d_v position. Although not shown in Fig. 10, we also perform other EQE simulations by changing the x_1 and x_2 values. These simulation results reveal that the EQE response is not sensitive to these parameters. Accordingly, it is obvious that the effect of x_v is far larger than that of the other parameters (x_1, x_2, d_v, ω_1, ω_2).

Figure 11 shows the EQE spectra obtained with variation of the (a) CIGS, (b) ZnO:Al, and (c) CdS layer thicknesses, and the corresponding changes in J_{SC} are shown in Figs. 11(d), 11(e), and 11(f), respectively. The parameter values used in this simulation are extracted from our CIGS structure, and only the layer thickness indicated in Figs. 11(a)–11(c) is changed. In the simulation of Fig. 11(a), the CIGS layer thickness is reduced from 1800 to 300 nm, while keeping the relative shape of $x_{\mathrm{sim}}(d)$ unchanged. Specifically, the (x_1, x_2, x_v) values are fixed in the simulation and (d_v, ω_1, ω_2) are reduced with the same ratio as the total CIGS layer thickness decreases. It can be seen from Fig. 11(a) that the EQE in the longer-wavelength region increases drastically when the light-absorber thickness increases up to 900 nm, and the J_{SC} value gradually saturates at $d > 900$ nm. In Fig. 11(d), the variation of J_{SC} with the CIGS layer thickness is shown together with the cases when the light-absorber layers are CIS and $CuGaSe_2$ (CGS) in Fig. 3(a). In our simulation, the J_{SC} obtained at different d values fluctuates slightly, as

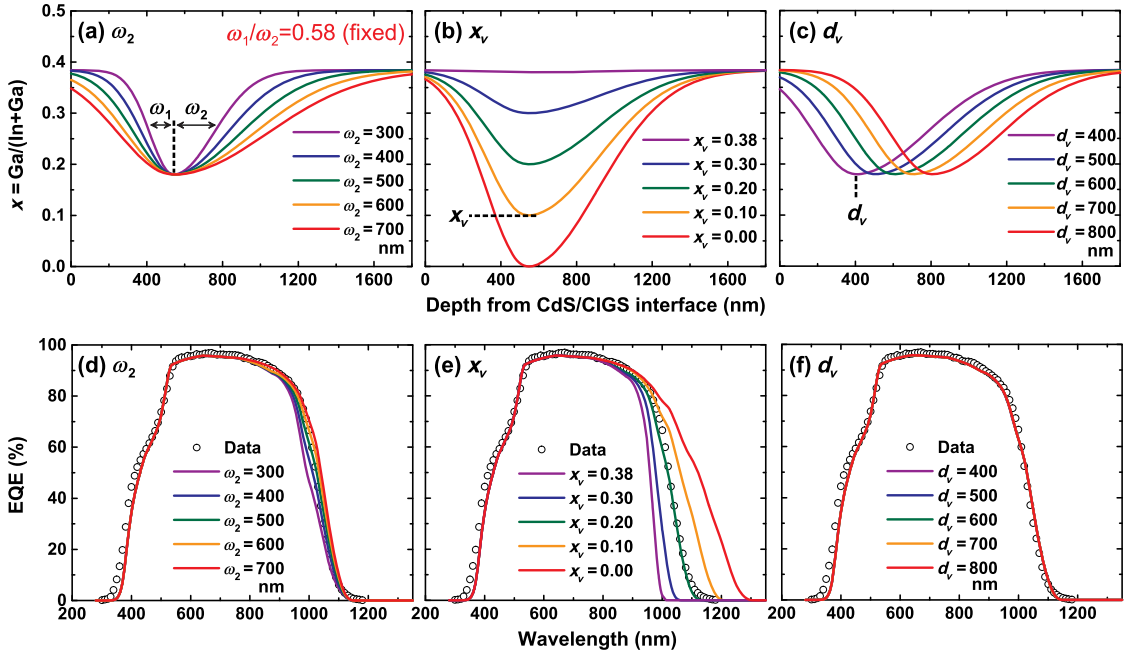

FIG. 10. EQE simulation results for different $x_{\mathrm{sim}}(d)$ profiles obtained with variation of (a) ω_2, (b) x_v, and (c) d_v. The EQE spectra calculated from the profiles of (a), (b), and (c) are shown in (d), (e), and (f), respectively.

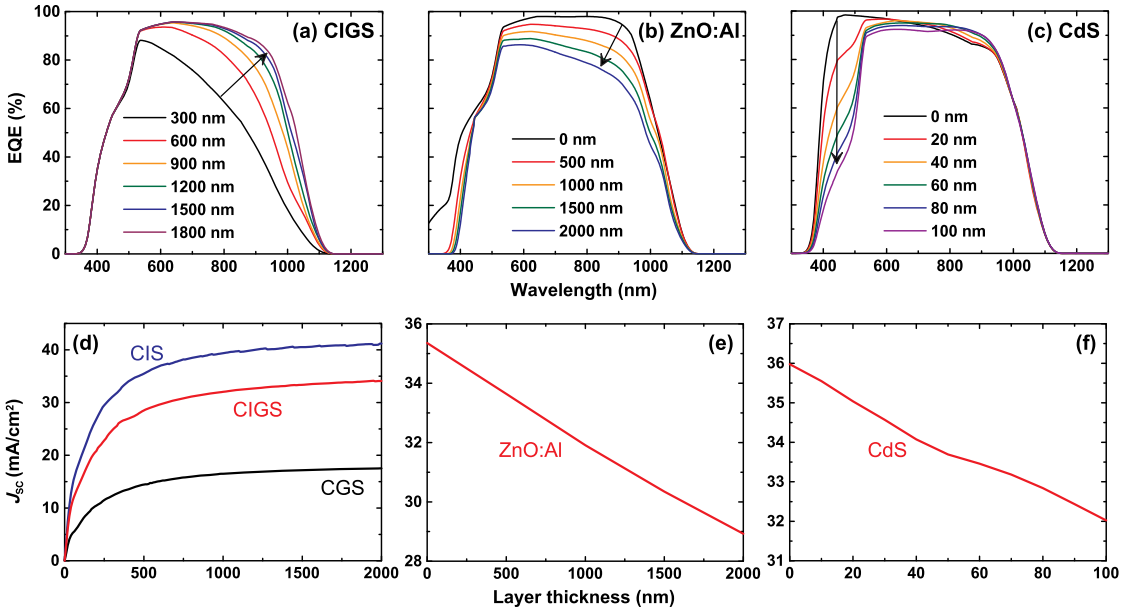

FIG. 11. EQE spectra obtained with variation of the (a) CIGS, (b) ZnO:Al, and (c) CdS layer thicknesses. The corresponding changes in J_{SC} are shown in (d), (e), and (f), respectively.

QE_{app} changes slightly depending on the choice of the minimum reflectance positions in R_{flat}. As confirmed from Fig. 11(d), J_{SC} increases with d and saturates at $d > 1$ μm. This trend is identical to that shown in Fig. 8(b). Quite naturally, the J_{SC} of the CIGS layer is intermediate between the CIS and CGS cases. As the E_g of the absorber layer increases, the maximum J_{SC} decreases from 41.2 mA/cm^2 (CIS) to 17.5 mA/cm^2 (CGS).

In Fig. 11(b), with increasing thickness of the ZnO:Al layer, the EQE in the visible-infrared region decreases gradually because of the increase in the free carrier absorption. When the CdS layer thickness increases, the EQE at $\lambda = 400$–540 nm deteriorates severely. From the EQE in this region, the CdS layer thickness can be determined rather easily. Previously, similar variations of the EQE spectrum with increasing CdS layer thickness have been reported [11,22,23]. The variation in CdS thickness also modifies the interference pattern in the visible-infrared regime, and the EQE in the region of $\lambda = 800$–1000 nm increases with the CdS layer thickness up to 60 nm.

V. DISCUSSION

A. Effect of Ga profile and thickness of the CIGS layer on EQE

Our calculation results indicate clearly that the light absorption in the CIGS layer occurs predominantly in the region of $d < 600$ nm. In actual thin CIGS solar cells, however, J_{SC} decreases largely from 30 mA/cm^2 ($d = 1000$ nm) to 22 mA/cm^2 ($d = 500$ nm) [10,32]. This effect is attributed to the strong carrier recombination at the CIGS/Mo interface [10,16,18,31,32,34]. In particular, as the CIGS layer becomes thinner, more light is absorbed near the CIGS/Mo interface, which, in turn, increases the carrier recombination loss in the highly defective interface region. As confirmed previously [5–7,9,10,13,16,18,31,32,34], the increasing Ga composition toward the defective Mo interface is quite effective in improving solar-cell characteristics. Since the position of the conduction-band minimum moves toward higher energies with increasing x [79,80], the conduction-band grading structure is formed by the backside Ga profile [5,6,8,9,13,34]. If we assume that the CIGS bottom region is located away from the space charge region formed near the CdS/CIGS interface, the effective energy barrier for the diffusing electrons is estimated roughly to be 0.14 eV from the E_g difference between x_2 and x_v in Fig. 4.

The above result indicates that, although most of the carriers are generated near the CdS/CIGS interface, the 1-μm-thick CIGS bottom layer having higher Ga compositions plays an important role as a back-surface field (BSF) layer suppressing the electron diffusion toward the defective CIGS(p)/Mo interface region [5,6,8–10,13,16,32,34], similar to the c-Si(p^+) BSF layer introduced at the c-Si(p)/Al interface in standard c-Si solar cells [81]. As shown in Fig. 11(d), J_{SC} saturates at $d_{sat} \sim 1000$ nm and, if the BSF layer thickness d_{BSF} is equivalent to the diffusion length (L_D) of the electrons in the CIGS layer, a total thickness of $d_{sat} + d_{BSF}$ is necessary to maximize J_{SC}. Since L_D of the CIGS layer is approximately 1 μm [10,13,14,18,31,34], this could explain the optimum CIGS layer thickness of 2 μm. It should be noted that, even though the d_v variation does not change the EQE

spectrum in Fig. 10(f), the enhanced recombination at the CIGS/Mo interface for higher d_v is expected to lower J_{SC} in actual devices. In addition, since the position of carrier generation within the CIGS layer totally depends on α of the CIGS layer, various results obtained from numerical device simulations need to be compared according to the optical constants applied in the calculations.

An important observation in the Ga-profile simulation of Fig. 10 is that the long-wavelength EQE response is predominantly determined by x_v in the profile. Since d_p of the CIGS layer is approximately 200 nm ($x \sim 0.4$, $E = 2.0$ eV), the infrared light is absorbed effectively near d_v even if the effective thickness of the x_v layer is quite thin. In other words, the absolute J_{SC} value in CIGS solar cells is controlled mainly by x_v. As indicated in Fig. 10(d), for a further increase in J_{SC}, the U-shaped Ga profile is preferable to the V-shaped profile, although its effect is rather limited.

As pointed out previously [5–9], V_{OC} improves by increasing E_g near the CdS/CIGS interface (i.e., x_1 in Fig. 4) because of the suppression of the front interface recombination. Thus, a larger x_1 value is expected to improve V_{OC}, whereas a lower x_v is preferable for enhanced light absorption. When the difference of x_1 and x_v is significant, however, a large electron barrier is generated by the front Ga grading, and carrier extraction from the CIGS layer becomes difficult [8]. Thus, for the front profile, a trade-off may exist between J_{SC} and V_{OC} for the different combination of (x_1, x_v).

B. Parasitic light absorption in ZnO:Al, CdS, and Mo layers

In CIGS modules, a thicker TCO layer is generally necessary to reduce the series resistance [20,36], as the application of metal grid electrodes is difficult in large-area modules. The thicker TCO layers, however, lead to the reduction in J_{SC}, as shown in Fig. 11(e). The effect of free carrier absorption also becomes significant for the CIGS layer with lower x_v values, as the EQE response in the solar cells extends toward the longer-wavelength region, where the free carrier absorption is more pronounced. It should be noted that the free carrier absorption expressed by (A_D, Γ_D) in Eqs. (6) and (7) increases at higher N_{opt} and lower μ_{opt}. Accordingly, a TCO layer with low N_{opt} and high μ_{opt} is quite beneficial for the reduction of the free carrier absorption, even if the resistivity $\rho_{opt} = 1/(eN_{opt}\mu_{opt})$ is constant. For this purpose, ZnO:B layers [19–21] that show higher μ_{opt} compared with ZnO:Al, have also been employed in a CIGS module production [20,21].

The EQE calculation results shown in Figs. 6, 8, and 9 indicate clearly that the presence of the CdS layer is quite detrimental for CIGS solar cells. In our simulation, only carrier collection in the CIGS-based light absorber is considered, and QE_{tex} obtained under this assumption shows excellent agreement with QE_{ex}. This result confirms that carrier extraction from the CdS layer is negligible and that all carriers generated within the CdS layer are lost through electron-hole recombination, most likely due to the formation of the defective CdS structure by the CBD technique. Thus, the CdS layer incorporated into CIGS solar cells can be considered as a "dead layer," similar to the hydrogenated amorphous silicon (a-Si:H) p layers in a-Si:H/c-Si heterojunction solar cells [82]. As reported previously [22], with increasing CdS layer thickness, V_{OC} and FF of the CIGS solar cells increase, whereas J_{SC} decreases gradually. Thus, there is a trade-off between (V_{OC}, FF) and J_{SC} for the CdS layer thickness. In general, the optimum CdS layer thickness is approximately 50 nm, and due to the island growth of the CdS layer in the CBD process [22], further reduction of the CdS layer thickness appears to be difficult. To suppress parasitic light absorption in the CdS layer, various buffer layers including In_2S_3 [1,15], Zn(O, S, OH) [1,20,21], Zn(O, S) [17], and ZnS [36] layers have been applied so far.

As mentioned earlier, the Mo layer exhibits the largest parasitic absorption among the solar-cell component layers. This originates from the simple fact that the reflectivity is quite low at the CIGS/($MoSe_2$)/Mo interface. In particular, the reflectivity of the CIGS/Mo interface is only 40% at $\lambda = 1100$ nm [25,26]. The high reflectivity at the metal back electrode becomes more critical in achieving higher efficiencies in thinner CIGS solar cells. To improve the reflectivity at the CIGS-metal interface, various materials are applied [24–26]. So far, for the ZrN [25] and Au [26] back-contact materials, the increase in J_{SC} is confirmed. Unfortunately, rather complicated processes are necessary when these contact materials are employed; in the case of the ZrN, the formation of a NaF precursor layer is required, as the ZrN acts as a diffusion barrier for Na [25], whereas the Au layer is formed on the CIGS back side after the lift-off process of the CIGS layer from the Mo-glass substrate [26]. Accordingly, there are as yet no simple metal back-contact materials that ensure (i) high reflectivity, (ii) good interface properties with CIGS layers, and (iii) sufficient Na diffusion.

On the other hand, the back-side reflection can be enhanced by incorporating a TCO back-reflector structure into the solar cell. In the case of a-Si:H-based solar cells, for example, an a-Si:H/ZnO/Ag rear structure has been widely adopted to increase the back-side reflection [83,84]. In fact, a previous optical simulation study performed for CIGS solar cells showed a large improvement of J_{SC} by 2 mA/cm^2 in a CIGS/ZnO/Ag structure [29]. In actual CIGS processes on TCO, however, the growth of an unintended Ga_2O_3 layer, which leads to a severe FF reduction, has been reported [28], and the formation of $MoSe_2$ contact and NaF precursor layers is required [18,27,28]. One possible transparent material for the CIGS back-reflector structure is MoO_x, which has a wide E_g of approximately 3 eV [85]. This material has already

been applied for CIGS solar cells [30], and J_{SC} could be improved by using a CIGS/MoO_x/Mo structure, although further study is necessary.

VI. CONCLUSION

We perform an explicit calculation of the EQE spectra for CIGS-based solar cells fabricated by a standard three-stage process. In our EQE simulation, to incorporate the effects of light scattering by the natural texture of the CIGS, an experimental reflectance spectrum obtained directly from the actual solar-cell structure is employed, whereas the absorptance spectra of each solar-cell component layer are determined from the optical-admittance method assuming a perfectly flat optical model. Moreover, based on a complete CIGS optical database established recently, the optical effect of the V-shaped Ga-compositional profile in the CIGS layers is calculated assuming an asymmetric double-Gaussian profile. For the modeling of the solar cells, we employ layer thicknesses and optical constants determined from transmission electron microscopy and spectroscopic ellipsometry analyses, respectively. Our simulation method provides an excellent fitting to the experimental EQE spectra of CIGS solar cells. Furthermore, by imposing the antireflection condition for a reflectance spectrum calculated assuming a flat optical model, an accurate EQE simulation becomes possible without the use of an experimental reflectance spectrum.

From the developed technique, the partial EQE and absorptance for depth from the interface and wavelength are determined. The partial EQE simulation reveals that the light absorption in the CIGS layer occurs predominantly within the 600-nm-thick CIGS layer near the CdS/CIGS interface, although the α values of our CIGS optical database ($\alpha = 6.6 \times 10^4$ cm^{-1} at 2.0 eV for CIS) are much lower than those reported earlier. As a result, the EQE contribution from the CIGS bottom layer (1 μm) is negligible, confirming that the CIGS bottom layer plays a dominant role as a back-surface field layer with the conduction-band grading.

Our absorptance calculation for the CIGS solar cell further indicates that the major parasitic light absorption occurs in the ZnO:Al, CdS, and Mo layers with a J_{SC} loss of approximately 3 mA/cm^2 in each layer. In particular, for the CdS layer, almost no carrier extraction is confirmed, indicating that this layer is an optically dead layer in the solar cells. The optical loss induced by the free carrier absorption in the ZnO:Al layer becomes significant in the longer-wavelength region. Among the solar-cell layers, however, the Mo layer shows the largest parasitic absorption. Thus, the introduction of a more highly reflective metal layer or a back-reflector structure is important for further improvement of J_{SC}.

Our EQE simulations performed for different Ga profiles show that the long-wavelength EQE response is preliminarily determined by a bottom Ga composition in the V-shaped profile even if the thickness of the Ga bottom region is only 200 nm. From an optical point of view, therefore, the thickness of the CIGS light-absorber layer can be reduced drastically to improve productivity. We further determined the effects of the CIGS-based absorber, ZnO:Al, and CdS layer thicknesses on the EQE spectrum. Based on our simulation technique, the EQE spectra of CIGS solar cells can be calculated rather easily without the requirement of intensive computer modeling for surface and interface structures. Accordingly, the developed technique provides a promising method for the quantitative analysis of optical loss and gain in CIGS thin-film solar cells.

ACKNOWLEDGMENTS

The authors would like to thank Dr. H. Shibata and Dr. Y. Kamikawa of the National Institute of Advanced Industrial Science and Technology (AIST) for their helpful discussions.

[1] For a review, see S. Niki, M. Contreras, I. Repins, M. Powalla, K. Kushiya, S. Ishizuka, and K. Matsubara, CIGS absorbers and processes, Prog. Photovoltaics **18**, 453 (2010).

[2] J. S. Ward, K. Ramanathan, F. S. Hasoon, T. J. Coutts, J. Keane, M. A. Contreras, T. Moriarty, and R. Noufi, A 21.5% efficient Cu(In, Ga)Se_2 thin-film concentrator solar cell, Prog. Photovoltaics **10**, 41 (2002).

[3] P. Jackson, D. Hariskos, E. Lotter, S. Paetel, R. Wuerz, R. Menner, W. Wischmann, and M. Pawalla, New world record efficiency for Cu(In, Ga)Se_2 thin-film solar cells beyond 20%, Prog. Photovoltaics **19**, 894 (2011).

[4] A. M. Gabor, J. R. Tuttle, D. S. Albin, M. A. Contreras, R. Noufi, and A. M. Hermann, High-efficiency $CuIn_xGa_{1-x}Se_2$ solar cells made from $(In_x, Ga_{1-x})_2Se_3$ precursor films, Appl. Phys. Lett. **65**, 198 (1994).

[5] A. M. Gabor, J. R. Tuttle, M. H. Bode, A. Franz, A. L. Tennant, M. A. Contreras, R. Noufi, D. G. Jensen, and A. M. Hermann, Band-gap engineering in Cu(In, Ga)Se_2 thin films grown from $(In, Ga)_2Se_3$ precursors, Sol. Energy Mater. Sol. Cells **41–42**, 247 (1996).

[6] M. A. Contreras, J. Tuttle, A. Gabor, A. Tennant, K. Ramanathan, S. Asher, A. Franz, J. Keane, L. Wang, and R. Noufi, High efficiency graded bandgap thin-film polycrystalline Cu(In, Ga)Se_2-based solar cells, Sol. Energy Mater. Sol. Cells **41–42**, 231 (1996).

[7] T. Dullweber, U. Rau, M. A. Contreras, R. Noufi, and H. Schock, Photogeneration and carrier recombination in graded gap Cu(In, Ga)Se_2 solar cells, IEEE Trans. Electron Devices **47**, 2249 (2000).

[8] A. Chirila, S. Buecheler, F. Pianezzi, P. Bloesch, C. Gretener, A. R. Uhl, C. Fella, L. Kranz, J. Perrenoud, S. Seyrling, R. Verma, S. Nishiwaki, Y. E. Romanyuk, G. Bilger, and A. N. Tiwari, Highly efficient Cu(In, Ga)Se_2 solar cells grown on flexible polymer films, Nat. Mater. **10**, 857 (2011).

[9] J. Song, S. S. Li, C. H. Huang, O. D. Crisalle, and T. J. Anderson, Device modeling and simulation of the performance of $Cu(In_{1-x}, Ga_x)Se_2$ solar cells, Solid State Electron. **48**, 73 (2004).

[10] M. Gloeckler and J. R. Sites, Potential of submicrometer thickness $Cu(In, Ga)Se_2$ solar cells, J. Appl. Phys. **98**, 103703 (2005).

[11] P. Chelvanathan, M. I. Hossain, and N. Amin, Performance analysis of copper-indium-gallium-diselenide (CIGS) solar cells with various buffer layers by SCAPS, Curr. Appl. Phys. **10**, S387 (2010).

[12] P. Aryal, J. Chen, Z. Huang, L. R. Dahal, M. N. Sestak, D. Attygalle, R. Jacobs, V. Ranjan, S. Marsillac, and R. W. Collins, Quantum efficiency simulations from on-line compatible mapping of thin-film solar cells, in *Proceedings of the 37th IEEE Photovoltaic Specialists Conference* (IEEE, New York, 2011), p. 2241.

[13] M. Troviano and K. Taretto, Analysis of internal quantum efficiency in double-graded bandgap solar cells including sub-bandgap absorption, Sol. Energy Mater. Sol. Cells **95**, 821 (2011).

[14] J. Pettersson, C. Platzer-Bjorkman, U. Zimmermann, and M. Edoff, Baseline model of graded-absorber $Cu(In, Ga)Se_2$ solar cells applied to cells with $Zn_{1-x}Mg_xO$ buffer layers, Thin Solid Films **519**, 7476 (2011).

[15] M. Richter, C. Schubbert, P. Eraerds, I. Riedel, J. Keller, J. Parisi, T. Dalibor, and A. Avellan-Hampe, Optical characterization and modeling of $Cu(In, Ga)(Se, S)_2$ solar cells with spectroscopic ellipsometry and coherent numerical simulation, Thin Solid Films **535**, 331 (2013).

[16] S. Ouedraogo, F. Zougmore, and J. M. Ndjaka, Numerical analysis of copper-indium-gallium-diselenide-based solar cells by SCAPS-1D, Int. J. Photoenergy **2013**, 1 (2013).

[17] J. Pettersson, T. Torndahl, C. Platzer-Bjorkman, A. Hultqvist, and M. Edoff, The influence of absorber thickness on $Cu(In, Ga)Se_2$ solar cells with different buffer layers, IEEE J. Photovoltaics **3**, 1376 (2013).

[18] J. Mattheis, P. J. Rostan, U. Rau, and J. H. Werner, Carrier collection in $Cu(In, Ga)Se_2$ solar cells with graded band gaps and transparent ZnO:Al back contacts, Sol. Energy Mater. Sol. Cells **91**, 689 (2007).

[19] Y. Hagiwara, T. Nakada, and A. Kunioka, Improved J_{sc} in CIGS thin film solar cells using a transparent conducting ZnO:B window layer, Sol. Energy Mater. Sol. Cells **67**, 267 (2001).

[20] K. Kushiya, M. Ohshita, I. Hara, Y. Tanaka, B. Sang, Y. Nagoya, M. Tachiyuki, and O. Yamase, Yield issues on the fabrication of 30 cm × 30 cm-sized $Cu(In, Ga)Se_2$-based thin-film modules, Sol. Energy Mater. Sol. Cells **75**, 171 (2003).

[21] K. Kushiya, Y. Tanaka, H. Hakuma, Y. Goushi, S. Kijima, T. Aramoto, and Y. Fujiwara, Interface control to enhance the fill factor over 0.70 in a large-area CIS-based thin-film PV technology, Thin Solid Films **517**, 2108 (2009).

[22] M. A. Contreras, M. J. Romero, B. To, F. Hasoon, R. Noufi, S. Ward, and K. Ramanathan, Optimization of CBD CdS process in high-efficiency $Cu(In, Ga)Se_2$-based solar cells, Thin Solid Films **403–404**, 204 (2002).

[23] K. Orgassa, U. Rau, Q. Nguyen, H. W. Schock, and J. H. Werner, Role of the CdS buffer layer as an active optical element in $Cu(In, Ga)Se_2$ thin-film solar cells, Prog. Photovoltaics **10**, 457 (2002).

[24] K. Orgassa, H. W. Schock, and J. H. Werner, Alternative back contact materials for thin film $Cu(In, Ga)Se_2$ solar cells, Thin Solid Films **431–432**, 387 (2003).

[25] J. Malmstrom, S. Schleussner, and L. Stolt, Enhanced back reflectance and quantum efficiency in $Cu(In, Ga)Se_2$ thin film solar cells with a ZrN back reflector, Appl. Phys. Lett. **85**, 2634 (2004).

[26] Z. J. Li-Kao, N. Naghavi, F. Erfurth, J. F. Guillemoles, I. Gerard, A. Etcheberry, J. L. Pelouard, S. Collin, G. Voorwinden, and D. Lincot, Towards ultrathin copper indium gallium diselenide solar cells: Proof of concept study by chemical etching and gold back contact engineering, Prog. Photovoltaics **20**, 582 (2012).

[27] P. J. Rostan, J. Mattheis, G. Bilger, U. Rau, and J. H. Werner, Formation of transparent and ohmic $ZnO:Al/MoSe_2$ contacts for bifacial $Cu(In, Ga)Se_2$ solar cells and tandem structures, Thin Solid Films **480–481**, 67 (2005).

[28] T. Nakada, Microstructural and diffusion properties of CIGS thin film solar cells fabricated using transparent conducting oxide back contacts, Thin Solid Films **480–481**, 419 (2005).

[29] A. Campa, J. Krc, J. Malmstrom, M. Edoff, F. Smole, and M. Topic, The potential of textured front ZnO and flat TCO/metal back contact to improve optical absorption in thin $Cu(In, Ga)Se_2$ solar cells, Thin Solid Films **515**, 5968 (2007).

[30] J. K. Larsen, H. Simchi, P. Xin, K. Kim, and W. N. Shafarman, Backwall superstrate configuration for ultrathin $Cu(In, Ga)Se_2$ solar cells, Appl. Phys. Lett. **104**, 033901 (2014).

[31] T. Dullweber, O. Lundberg, J. Malmstrom, M. Bodegard, L. Stolt, U. Rau, H. W. Schock, and J. H. Werner, Back surface band gap gradings in $Cu(In, Ga)Se_2$ solar cells, Thin Solid Films **387**, 11 (2001).

[32] O. Lundberg, M. Bodegard, J. Malmstrom, and L. Stolt, Influence of the $Cu(In, Ga)Se_2$ thickness and Ga grading on solar cell performance, Prog. Photovoltaics **11**, 77 (2003).

[33] Z. Jehl, F. Erfurth, N. Naghavi, L. Lombez, I. Gerard, M. Bouttemy, P. Tran-Van, A. Etcheberry, G. Voorwinden, B. Dimmler, W. Wischmann, M. Powalla, J. F. Guillemoles, and D. Lincot, Thinning of CIGS solar cells: Part II: Cell characterizations, Thin Solid Films **519**, 7212 (2011).

[34] O. Lundberg, M. Edoff, and L. Stolt, The effect of Ga-grading in CIGS thin film solar cells, Thin Solid Films **480–481**, 520 (2005).

[35] R. Kniese, D. Hariskos, G. Voorwinden, U. Rau, and M. Powalla, High band gap $Cu(In, Ga)Se_2$ solar cells and modules prepared with in-line co-evaporation, Thin Solid Films **431–432**, 543 (2003).

[36] M. Powalla, G. Voorwinden, D. Hariskos, P. Jackson, and R. Kniese, Highly efficient CIS solar cells and modules made by the co-evaporation process, Thin Solid Films **517**, 2111 (2009).

[37] M. Agrawal and M. Frei, Rigorous optical modeling and optimization of thin-film photovoltaic cells with textured transparent conductive oxides, Prog. Photovoltaics **20**, 442 (2012).

[38] S. C. Baker-Finch and K. R. McIntosh, Reflection of normally incident light from silicon solar cells with pyramidal texture, Prog. Photovoltaics **19**, 406 (2011).

[39] C. Haase and H. Stiebig, Optical properties of thin-film silicon solar cells with grating couplers, Prog. Photovoltaics **14**, 629 (2006).

[40] C. Haase and H. Stiebig, Thin-film silicon solar cells with efficient periodic light trapping texture, Appl. Phys. Lett. **91**, 061116 (2007).

[41] O. Isabella, S. Solntsev, D. Caratelli, and M. Zeman, 3-D optical modeling of thin-film silicon solar cells on diffraction gratings, Prog. Photovolt., doi:10.1002/pip.1257 (2012).

[42] C. A. Durante Rincon, E. Hernandez, M. I. Alonso, M. Garriga, S. M. Wasim, C. Rincon, and M. Leon, Optical transitions near the band edge in bulk $CuIn_xGa_{1-x}Se_2$ from ellipsometric measurements, Mater. Chem. Phys. **70**, 300 (2001).

[43] M. I. Alonso, M. Garriga, C. A. Durante Rincon, E. Hernandez, and M. Leon, Optical functions of chalcopyrite $CuGa_xIn_{1-x}Se_2$ alloys, Appl. Phys. A **74**, 659 (2002).

[44] K. Orgassa, U. Rau, H. W. Schock, and J. H. Werner, Optical constants of $Cu(In, Ga)Se_2$ thin films from normal incidence transmittance and reflectance, in *Proceedings of the 3rd World Conference on Photovoltaic Energy Conversion* (WCPEC-3, Osaka, 2003), 2P-A8-04.

[45] P. D. Paulson, R. W. Birkmire, and W. N. Shafarman, Optical characterization of $CuIn_{1-x}Ga_xSe_2$ alloy thin films by spectroscopic ellipsometry, J. Appl. Phys. **94**, 879 (2003).

[46] S. Theodoropoulou, D. Papadimitriou, K. Anestou, C. Cobet, and N. Esser, Optical properties of $CuIn_{1-x}Ga_xSe_2$ quaternary alloys for solar-energy conversion, Semicond. Sci. Technol. **24**, 015014 (2009).

[47] P. Aryal, D. Attygalle, P. Pradhan, N. J. Podraza, S. Marsillac, and R. W. Collins, Large area compositional mapping of $Cu(In_{1-x}Ga_x)Se_2$ materials and devices with spectroscopic ellipsometry, IEEE J. Photovoltaics **3**, 359 (2013).

[48] S. Minoura, K. Kodera, T. Maekawa, K. Miyazaki, S. Niki, and H. Fujiwara, Dielectric function of $Cu(In, Ga)Se_2$-based polycrystalline materials, J. Appl. Phys. **113**, 063505 (2013).

[49] H. A. Macleod, *Thin-Film Optical Filters* (CRC Press, New York, 2010).

[50] J. A. Berning and P. H. Berning, Thin films calculations using the IBM 650 electronic calculator, J. Opt. Soc. Am. **50**, 813 (1960).

[51] A. Y. Darkwi, W. K. Loke, and K. Ibrahim, Computer simulation of collection efficiency of *a*-Si:H tandem solar cells interconnected by transparent conductive oxide, Sol. Energy Mater. Sol. Cells **60**, 1 (2000).

[52] W. Horig, H. Neumann, and H. Sobotta, The optical properties of $CuInSe_2$ thin films, Thin Solid Films **48**, 67 (1978).

[53] C. Guillen and J. Herrero, Effects of thermal and chemical treatments on the composition and structure of electrodeposited $CuInSe_2$ thin films, J. Electrochem. Soc. **141**, 225 (1994).

[54] C. Guillen and J. Herrero, Improvement of the optical properties of electrodeposited $CuInSe_2$ thin films by thermal and chemical treatments, Sol. Energy Mater. Sol. Cells **43**, 47 (1996).

[55] Y. Hashimoto, N. Kohara, T. Negami, N. Nishitani, and T. Wada, Chemical bath deposition of CdS buffer layer for CIGS solar cells, Sol. Energy Mater. Sol. Cells **50**, 71 (1998).

[56] T. Wada, N. Kohara, S. Nishiwaki, and T. Negami, Characterization of the $Cu(In, Ga)Se_2$/Mo interface in CIGS solar cells, Thin Solid Films **387**, 118 (2001).

[57] J. Krc, M. Zeman, F. Smole, and M. Topic, Optical modeling of *a*-Si:H solar cells deposited on textured glass/SnO_2 substrates, J. Appl. Phys. **92**, 749 (2002).

[58] See the Supplemental Material at http://link.aps.org/supplemental/10.1103/PhysRevApplied.2.034012 for the numerical values of all the optical constants in Fig. 3.

[59] P. G. Snyder, J. A. Woollam, S. A. Alterovitz, and B. Johs, Modeling $Al_xGa_{1-x}As$ optical constants as functions of composition, J. Appl. Phys. **68**, 5925 (1990).

[60] J. Chen, J. Li, D. Sainju, K. D. Wells, N. J. Podraza, and R. W. Collins, Multilayer Analysis of the CdTe Solar Cell Structure by Spectroscopic Ellipsometry, in *Proceedings of the IEEE 4th World Conference on Photovoltaic Energy Conversion* (IEEE, New York, 2006), p. 711.

[61] J. E. Jaffe and A. Zunger, Electronic structure of the ternary chalcopyrite semiconductors $CuAlS_2$, $CuGaS_2$, $CuInS_2$, $CuAlSe_2$, $CuGaSe_2$, and $CuInSe_2$, Phys. Rev. B **28**, 5822 (1983).

[62] J. E. Jaffe and A. Zunger, Theory of the band-gap anomaly in ABC_2 chalcopyrite semiconductors, Phys. Rev. B **29**, 1882 (1984).

[63] H. Fujiwara, *Spectroscopic Ellipsometry: Principles and Applications* (Wiley, West Sussex, 2007).

[64] H. Fujiwara and M. Kondo, Effects of carrier concentration on the dielectric function of ZnO:Ga and In_2O_3:Sn studied by spectroscopic ellipsometry: Analysis of free-carrier and band-edge absorption, Phys. Rev. B **71**, 075109 (2005).

[65] B. E. Sernelius, K.-F. Berggren, Z.-C. Jin, I. Hamberg, and C. G. Granqvist, Band-gap tailoring of ZnO by means of heavy Al doping, Phys. Rev. B **37**, 10244 (1988).

[66] Y. Tawada and H. Fujiwara, Light-induced conductivity enhancement in boron-doped zinc oxide thin films deposited by low-pressure chemical vapor deposition, Appl. Phys. Express **5**, 085802 (2012).

[67] K. Sago, H. Kuramochi, H. Iigusa, K. Utsumi, and H. Fujiwara, Ellipsometry characterization of polycrystalline ZnO layers with the modeling of carrier concentration gradient: Effects of grain boundary, humidity, and surface texture, J. Appl. Phys. **115**, 133505 (2014).

[68] T. Minami, H. Sato, K. Ohashi, T. Tomofuji, and S. Takata, Conduction mechanism of highly conductive and transparent zinc oxide thin films prepared by magnetron sputtering, J. Cryst. Growth **117**, 370 (1992).

[69] K. Ellmer, Resistivity of polycrystalline zinc oxide films: current status and physical limit, J. Phys. D **34**, 3097 (2001).

[70] G. E. Jellison, Jr. and F. A. Modine, Parameterization of the optical functions of amorphous materials in the interband region, Appl. Phys. Lett. **69**, 371 (1996); **69**, 2137(E) (1996).

[71] P. I. Rovira and R. W. Collins, Analysis of specular and textured SnO_2 : F films by high speed four-parameter Stokes vector spectroscopy, J. Appl. Phys. **85**, 2015 (1999).

[72] H. Yu, H. Qi, Y. Cui, Y. Shen, J. Shao, and Z. Fan, Influence of substrate temperature on properties of MgF_2 coatings, Appl. Surf. Sci. **253**, 6113 (2007).

[73] H. Kruger, E. Kemnitz, A. Hertwig, and U. Beck, Transparent MgF_2-films by sol-gel coating: Synthesis and optical properties, Thin Solid Films **516**, 4175 (2008).

[74] J. D. Walker, H. Khatri, V. Ranjan, J. Li, R. W. Collins, and S. Marsillac, Electronic and structural properties of molybdenum thin films as determined by real-time spectroscopic ellipsometry, Appl. Phys. Lett. **94**, 141908 (2009).

[75] D. Schmid, M. Ruckh, F. Grunwald, and H. W. Schock, Chalcopyrite/defect chalcopyrite heterojunctions on the basis of $CuInSe_2$, J. Appl. Phys. **73**, 2902 (1993).

[76] S. B. Zhang, S. Wei, and A. Zunger, Defect physics of the $CuInSe_2$ chalcopyrite semiconductor, Phys. Rev. B **57**, 9642 (1998).

[77] C. Persson and A. Zunger, Compositionally induced valence-band offset at the grain boundary of polycrystalline chalcopyrites creates a hole barrier, Appl. Phys. Lett. **87**, 211904 (2005).

[78] S. M. Sze, *Physics of Semiconductor Devices* (Wiley, New York, 1981).

[79] S. Wei, S. B. Zhang, and A. Zunger, Effects of Ga addition to $CuInSe_2$ on its electronic, structural, and defect properties, Appl. Phys. Lett. **72**, 3199 (1998).

[80] M. Turcu and U. Rau, Compositional trends of defect energies, band alignments, and recombination mechanisms in the $Cu(In, Ga)(Se, S)_2$ alloy system, Thin Solid Films **431–432**, 158 (2003).

[81] *Handbook of Photovoltaic Science and Engineering*, 2nd ed., edited by A. Luque and S. Hegedus (Wiley, West Sussex, 2011).

[82] H. Fujiwara and M. Kondo, Effects of *a*-Si:H layer thicknesses on the performance of *a*-Si:H/*c*-Si heterojunction solar cells, J. Appl. Phys. **101**, 054516 (2007).

[83] S. Guha, Material and device consideration for high efficiency *a*-Si alloy-based multijunction cells, J. Non-Cryst. Solids **198–200**, 1076 (1996).

[84] J. Muller, B. Rech, J. Springer, and M. Vanecek, TCO and light trapping in silicon thin film solar cells, Solar Energy **77**, 917 (2004).

[85] M. T. Greiner, M. G. Helander, W. Tang, Z. Wang, J. Qiu, and Z. Lu, Universal energy-level alignment of molecules on metal oxides, Nat. Mater. **11**, 76 (2012).